

# Theoretical and experimental error analysis of continuous-wave time-of-flight range cameras

**Mario Frank**

ETH Zurich  
Department of Computer Science  
Haldeneggsteig 4  
8092 Zurich, Switzerland

**Matthias Plaue**

Technische Universität Berlin  
Department of Mathematics  
Straße des 17. Juni 136  
10623 Berlin, Germany

**Holger Rapp**

Universität Karlsruhe  
Institut für Mess- und Regelungstechnik  
Engler-Bunte-Ring 21  
76131 Karlsruhe, Germany

**Ullrich Köthe**

**Bernd Jähne**

**Fred A. Hamprecht**  
University of Heidelberg  
Heidelberg Collaboratory for Image Processing  
Speyerer Straße 4  
69115 Heidelberg, Germany

**Abstract.** We offer a formal investigation of the measurement principle of time-of-flight 3-D cameras using correlation of amplitude-modulated continuous-wave signals. These sensors can provide both depth maps and IR intensity pictures simultaneously and in real time. We examine the theory of the data acquisition in detail. The variance of the range measurements is derived in a concise way and we show that the computed range follows an offset normal distribution. The impact of quantization of that distribution is discussed. All theoretically investigated errors like the behavior of the variance, depth bias, saturation and quantization effects are supported by experimental results. © 2009 Society of Photo-Optical Instrumentation Engineers. [DOI: 10.1117/1.3070634]

Subject terms: ranging; sensors; phase measurement.

Paper 080601R received Jul. 30, 2008; revised manuscript received Nov. 7, 2008; accepted for publication Nov. 16, 2008; published online Jan. 29, 2009.

## 1 Introduction

Laser scanners are an established and robust technology for the observation of 3-D scenes (e.g., Ref. 1). However, they rely on moving parts and can acquire a depth map only consecutively by scanning over the rows. In contrast, time-of-flight (TOF) 3-D cameras using correlation of amplitude-modulated active continuous-wave illumination can acquire entire depth maps and intensity images at once. An elaborate CMOS technology<sup>2-4</sup> detects and processes the signals on-chip in real time for all pixels simultaneously. These inexpensive sensors are now becoming a promising candidate for a wide range of applications, from industrial production surveillance to obstacle detection in the automotive sector. However, since the technique is fairly new, many available cameras still have a prototype character and some aspects of the underlying theory are not yet completely understood. This paper seeks to clarify by offering a theoretically sound and compact formulation of the signal genesis and of the algorithms that estimate range, amplitude and intensity. We show that the estimated range follows an offset normal distribution; and we study the im-

pact of the signal's modulation amplitude and the on-chip quantization on the computed range, both theoretically and experimentally.

The remainder of the paper is organized as follows. Section 2 references past work. In Sec. 3, the mathematical properties of the range acquisition are discussed in detail. Section 4 focuses on error propagation and systematic errors. In this context, the quantization error and its impact on the probability distribution of the range is investigated. Finally, Sec. 5 presents measurements that enable us to observe all the effects discussed.

## 2 Related Work

TOF systems using the correlation of amplitude-modulated continuous light to record 3-D scenes have been known<sup>5</sup> at least since 1976. In Ref. 5, the dependency of the range error on the signal amplitude was derived using Gaussian error propagation. Following this relation, it was proposed to adapt the number of samples that are used to estimate the phase as a function of the modulation amplitude.

In Ref. 6, a system using multiple diodes was introduced that obviated scanning and avoided moving mechanical parts. A range sensor that modulates the signal frequency was presented in Ref. 7. A very good overview of different active range finding concepts including amplitude-modulated continuous-wave sensors existing at that time

was given in Ref. 8. An overview of possible algorithms for phase computation from interferograms was presented in Ref. 9 in the context of phase measurement interferometry.

The first sensors using pixelwise on-chip correlation were presented in 1995 in Refs. 2 and 3. A good introduction to the working principle of a CMOS chip using amplitude-modulated continuous-wave correlation is given in Refs. 10 and 11, a short overview can be found in Ref. 12. In Ref. 13, measurements were performed to investigate the error as a function of the signal modulation amplitude. In Refs. 14–16, Gaussian error propagation was used to derive that dependency. A practical implementation of a chip-based range finder is presented in Ref. 17. A broad overview on laser radars that additionally to amplitude-correlated TOF sensors covers sensors for pulsed, chirped, and coherent signals is given in Ref. 18. In Ref. 19, applications for optical coherence tomography are shown that use the same phase estimation principle on another CMOS chip. The influence of nonorthogonal reflecting surfaces is discussed in Ref. 20. A calibration technique for TOF cameras is proposed in Ref. 21. Finally, the experimental setup from Sec. 5 was first described in Ref. 22.

### 3 Computation of Range, Amplitude, and Intensity

The basic principle of a TOF camera is to send out a signal and to measure the time required until its reflection can be detected by the camera. In contrast to systems with pulsed signals (e.g., Ref. 23), the described method makes use of modulated continuous light to determine that time. The modulated light (optical signal) emitted by IR diodes is reflected from a surface in the scene and returns after the TOF  $t_d$ . The TOF is proportional to the distance  $d = (c/2)t_d$  of the object surface from the camera, and to the phase delay:

$$\phi_d = \frac{4\pi f}{c}d, \quad (1)$$

of the optical signal that is correlated (mixed) with the reference signal of the same modulation frequency  $f$ . This method resembles the concept of phase shifting interferometry (PSI), where a coherent light beam interferes with a reference beam at several phase shifts to retrieve the phase: For each phase shift a different interferogram is obtained and from these so-called buckets the phase can be computed in several ways.<sup>9</sup> For 3-D TOF cameras, the concept is slightly different: The reference signal is electronic and has radio frequency. The signal drives the emitting diodes such that the amplitude of the optical signal is modulated with the same frequency. Opposed to methods based on optical interference, the emitted light does not have to be coherent, which avoids errors such as speckle noise<sup>24</sup> and allows for a cheap fabrication of such ranging systems. On the camera chip the backscattered optical signal is converted to an electronic signal and immediately correlated with the original reference signal at several phase shifts  $\alpha_n = (2\pi n/N)$ ,  $n=0, \dots, N-1$ . Each pixel acquires all  $N$  correlated signals for the computation of its range value. Without suitable unwrapping of the phase delay, the range can be measured unambiguously only up to the distance

corresponding to an angle of  $\phi_{d,\max} = 2\pi$ , i.e.,  $d_{\max} = (c/4\pi f)\phi_{d,\max} = c/(2f) = 7.5$  m.

The following calculations in this section derive the expressions for the correlated signal—the raw intensities or raw signal—assuming an arbitrary number of phase shifts and a general shape of the reference signal. In turn, formulas for retrieving the phase, amplitude, and intensity of the signal are derived assuming harmonic and anharmonic signals. For the measured raw intensities  $I_n$ ,  $n=1, \dots, N-1$ , the following (correlation) formula holds:

$$\begin{aligned} I_n &= \frac{1}{t'_1 - t'_0} \int_{t'_0}^{t'_1} R\left(t - \frac{\alpha_n}{2\pi f}\right) S(t + t_d) dt \\ &= \frac{1}{t_1 - t_0} \int_{t_0}^{t_1} R(t) S\left(t + \frac{\alpha_n}{2\pi f} + t_d\right) dt, \end{aligned} \quad (2)$$

where  $T = t'_1 - t'_0 = t_1 - t_0$  represents the integration time,  $S$  is the optical signal, and  $R$  is the reference signal.

Since both the optical signal  $S$  and the reference signal  $R$  are modulated with the same frequency  $f = \omega/(2\pi)$ , it is natural to expand both of them into a Fourier series:

$$R(t) = \sum_{j=-\infty}^{\infty} R_j \exp(ij\omega t), \quad S(t) = \sum_{k=-\infty}^{\infty} S_k \exp(ik\omega t). \quad (3)$$

Plugging both series into the correlation formula leads to

$$\begin{aligned} I_n &= \frac{1}{t_1 - t_0} \int_{t_0}^{t_1} \sum_{j=-\infty}^{\infty} \sum_{k=-\infty}^{\infty} R_j S_k e^{ij\omega t} e^{ik\omega(t + \frac{\alpha_n}{\omega} + t_d)} dt \\ &= \sum_{j=-\infty}^{\infty} \sum_{k=-\infty}^{\infty} R_j S_k e^{ik(\alpha_n + \omega t_d)} \underbrace{\frac{1}{t_1 - t_0} \int_{t_0}^{t_1} e^{i(j+k)\omega t} dt}_{=: \eta} \end{aligned} \quad (4)$$

If  $j = -k$ , the term  $\eta$  computes to  $t_1 - t_0$ . If  $j \neq -k$ , we have

$$\eta = \frac{-i}{(t_1 - t_0)(j + k)\omega} \{\exp[i(j + k)\omega t_1] - \exp[i(j + k)\omega t_0]\}. \quad (5)$$

The maximal magnitude that this expression can take is  $2/[(t_1 - t_0)(j + k)\omega]$ . Since typical integration times  $t_1 - t_0 \approx 5$  ms are much larger than the modulation period  $(2\pi)/\omega = 50$  ns, the summands with  $j \neq -k$  are negligible. This can be interpreted as follows: the actual integration interval has no influence to the final intensity if the time is chosen to be long compared to the modulation frequency—even if the integration is not performed over whole periods. Thus, one finally arrives at

$$I_n \approx \sum_{k=-\infty}^{\infty} R_{-k} S_k \exp[ik(\alpha_n + \phi_d)]. \quad (6)$$

#### 3.1 Amplitude, Phase, and Offset of Harmonically Modulated Optical Signals

Assuming the optical signal and the reference signal to be harmonically modulated,

$$S(t) = c' + A' \cos(\omega t + \theta') = \frac{A'}{2} e^{-i\theta'} \exp(-i\omega t) + c' + \frac{A'}{2} e^{i\theta'} e^{i\omega t}, \quad (7)$$

the raw intensities are of the same form:

$$I_n = c + \frac{A}{2} \left\{ \exp\left(2\pi i \frac{n}{N}\right) \exp[i(\phi_d + \theta)] + \exp\left(-2\pi i \frac{n}{N}\right) \exp[-i(\phi_d + \theta)] \right\}, \quad (8)$$

$$= c + A \cos(\alpha_n + \phi_d + \theta),$$

where  $c = R_0 c'$ ,  $A = |R_1| A'$ , and  $\theta = \theta' - \arg(R_1)$ .

To recover the offset  $c$  (intensity), the phase delay  $\phi_d$  (range information) and the amplitude  $A$  (modulation amplitude) the following formulas can be used:

$$A = \frac{2}{N} \left| \sum_{n=0}^{N-1} I_n \exp\left(-2\pi i \frac{n}{N}\right) \right|, \quad (9)$$

$$\phi_d + \theta = \arg \left[ \sum_{n=0}^{N-1} I_n \exp\left(-2\pi i \frac{n}{N}\right) \right],$$

$$c = \frac{1}{N} \sum_{n=0}^{N-1} I_n.$$

This solution is optimal in the least-squares sense, since writing the expressions for the raw intensities in matrix notation yields

$$\begin{pmatrix} I_0 \\ \vdots \\ I_{N-1} \end{pmatrix} = \begin{pmatrix} 1 & 1 & 1 \\ w & \bar{w} & 1 \\ \vdots & \vdots & \vdots \\ w^{N-1} & \bar{w}^{N-1} & 1 \end{pmatrix} \begin{pmatrix} \frac{A}{2} z \\ \frac{A}{2} \bar{z} \\ c \end{pmatrix}, \quad (10)$$

with  $z = \exp[i(\phi_d + \theta)]$  and  $w = \exp(2\pi i/N)$ .

Using the fact that the  $w^n$ s are the  $N$ 'th roots of unity,<sup>†</sup> it is easy to see that the coefficient matrix  $\mathbf{B}$  that they constitute satisfies  $\mathbf{B}^* \mathbf{B} = \text{diag}(N, N, N)$ .

Thus, the Moore-Penrose inverse<sup>25</sup> of  $\mathbf{B}$  is  $(\mathbf{B}^* \mathbf{B})^{-1} \mathbf{B}^* = (1/N) \mathbf{B}^*$ , and the least-squares solution  $(Az, A\bar{z}, c)^T = (1/N) \mathbf{B}^* \mathbf{I}$  together with  $\phi_d + \theta = \arg(Az)$  and  $A = |Az|$  yields the preceding result. Note that this is a meaningful result only for  $N \geq 3$ —otherwise the number of equations does not suffice to determine a unique least squares solution.

<sup>\*</sup>Up to some constant phase offset  $\theta$  that can easily be eliminated by camera calibration. This offset is due to the time that the internal signal needs to propagate.

<sup>†</sup>In particular,  $\sum_{n=0}^{N-1} w^{kn} = 0$  for any integer  $k$ .

### 3.2 Anharmonic Modulated Signals

For nonharmonically modulated optical signals, the solution above is no longer valid. In Ref. 16 a formula for calculating the phase delay information from nonharmonic signals is derived with the help of an analytic regression argument. This formula is very similar to the expression for harmonic signals but involves the higher harmonics of the mixed signal. Here, we derive these results algebraically. Assume

$$I_n = c + \sum_{k=1}^l A_k \cos(k\alpha_n + k\phi_d + \theta_k) = c + \sum_{k=1}^l \frac{A_k}{2} [\exp(ik\alpha_n) \exp(ik\phi_d + i\theta_k) + \exp(-ik\alpha_n) \exp(-ik\phi_d - i\theta_k)], \quad (11)$$

with some maximal bandwidth  $l$ . This leads to the system of linear equations {the coefficient matrix is of dimensions  $[N \times (2l+1)]$ }:

$$\begin{pmatrix} I_0 \\ \vdots \\ I_{N-1} \end{pmatrix} = \begin{pmatrix} 1 & 1 & \cdots & 1 & 1 & 1 \\ w & \bar{w} & \cdots & w^l & \bar{w}^l & 1 \\ \vdots & \vdots & \cdots & \vdots & \vdots & \vdots \\ w^{N-1} & \bar{w}^{N-1} & \cdots & w^{l(N-1)} & \bar{w}^{l(N-1)} & 1 \end{pmatrix} \times \begin{pmatrix} \frac{A_1}{2} z_1 \\ \frac{A_1}{2} \bar{z}_1 \\ \vdots \\ \frac{A_l}{2} z_l \\ \frac{A_l}{2} \bar{z}_l \\ c \end{pmatrix}, \quad (12)$$

with  $z_k = \exp(ik\phi_d + i\theta_k)$  and  $w = \exp(2\pi i/N)$ .

By arguments similar to the preceding, the least-squares solution computes to the one stated in Ref. 11.<sup>‡</sup>

$$A_k = \frac{2}{N} \left| \sum_{n=0}^{N-1} I_n \exp\left(-2\pi i k \frac{n}{N}\right) \right|,$$

$$k\phi_d + \theta_k = \arg \left[ \sum_{n=0}^{N-1} I_n \exp\left(-2\pi i k \frac{n}{N}\right) \right],$$

<sup>‡</sup>By means of the formula  $\arg(x+iy) = \arctan(y/x)$ —which is only valid for vectors  $(x, y)$  with an angle in the interval  $[-\pi/2, \pi/2]$ .

$$c = \frac{1}{N} \sum_{n=0}^{N-1} I_n. \quad (13)$$

Again, this solution is only valid for  $N \geq 2l+1$ ; that is, if the signal has sufficiently low bandwidth compared to the number of sampling points—which is essentially the sampling theorem. For nonharmonically modulated signals, we propose to use some prior knowledge about the Fourier coefficients to obtain an improved estimator for the phase delay. This knowledge can be inferred from the actual wave forms of the optical signal and the reference signal. In this context, asymmetric wave forms pose a particular problem since the phase offsets  $\theta_k$  differ. Without knowing those offsets, the computation of the phase delay is impossible and it is necessary to model the range-phase relationship on empirical grounds.

#### 4 Error Analysis for Harmonically Modulated Signals

The raw values that are used to compute  $A$  and  $\phi$  are subject to noise. Hence, the modulation amplitude and the range information that one gets from the camera are noisy, as well. In the following section, we give an analysis of this resulting variance. There are different ways to derive it. In Sec. 4.1, we perform Gaussian error propagation for the four phase algorithm with four raw channels as in Refs. 16 and 26, but with a more compact notation using matrices. In principle, this derivation can also be performed with eight or more raw channels but becomes tedious then. In Sec. 4.2, we employ the probability distribution of the raw values and derive directly the resulting phase probability distribution and its spread for the four phase algorithm with four and eight raw channels, respectively. Both derivations neglect the fact that the raw intensities are quantized after the AD conversion. Finally, in Sec. 4.3, we discuss the impact of this quantization noise on the range bias and show numerically how it affects the probability distribution of the phase. Usually, quantization is considered to cause an error with uniformly distributed magnitude, which leads to a variance of  $1/12$  in units of the rounded numbers. However, since in the genesis of the phase data the rounded raw signals are further processed in a particular way, the impact of quantization can be much higher. Neglecting saturation effects due to overexposure—which can be considered as a technical deficiency rather than being caused by the algorithm itself—the noise and the quantization of the raw values are the factors affecting the quality of the range data the most.

##### 4.1 Gaussian Error Propagation for Four-Phase-Shifting Technique with Four Raw Channels

Once an algorithm for calculating the values for  $A$ ,  $\phi$ , and  $c$  or other quantities (such as amplitudes from higher Fourier modes for nonharmonically modulated signals) is chosen, those quantities can be regarded as functions  $f$  of the random vector of measurements  $I = (I_0, \dots, I_{N-1})^T$ . It is well-known<sup>27</sup> that the variance matrix of the random vector  $\mathbf{f}(I) = (A, \phi, c)^T$  can be computed approximately by  $\text{Var}[\mathbf{f}(I)] \approx Df(\mu) \text{Var}(I) Df(\mu)^T$ . Herein,  $Df$  is the Jacobian (first derivative) of  $f$  and  $\mu = \langle I \rangle$  is the mean of  $I$  which in

practice is substituted by the measured raw intensities or some other unbiased estimator  $\hat{\mu}$  based for example on averaging multiple frames.

Estimating the mean of  $f(I)$  by setting  $\langle f(I) \rangle = f(\hat{\mu})$  is generally biased.<sup>8</sup> For each component  $f_k$  this bias can be calculated approximately by<sup>11</sup>  $\text{Bias}_{f_k} \approx (1/2) \text{Trace}[\text{Hess}_{f_k}(\hat{\mu}) \text{Var}(I)]$ . Herein,  $\text{Hess}_{f_k}$  stands for the Hessian (second derivative) of the  $k$ 'th component of  $f$ .

Writing down the formulas for the offset, amplitude and total phase  $\phi = \phi_d + \theta$  for harmonically modulated signals specifically for the case  $N=4$ , one has

$$A = \frac{1}{2} |I_0 - I_2 + i(I_3 - I_1)|,$$

$$\phi = \arg[I_0 - I_2 + i(I_3 - I_1)],$$

$$c = \frac{1}{4} (I_0 + I_1 + I_2 + I_3). \quad (14)$$

Assuming  $\phi$  to take values in the interval  $[-\pi/2, \pi/2]$ , one can write  $\phi = \arctan [(I_3 - I_1)/(I_0 - I_2)]$ , which is the usual formula found in the literature. However, such a restriction is not permissible. Therefore, we use Eq. (14) to calculate phase delays in the whole unambiguous range  $]-\pi, \pi]$ .

Thus, we set  $f: \mathbb{R}^4 \rightarrow \mathbb{R}^+ \times S^1 \times \mathbb{R}$ ,  $f: I \mapsto (A, \phi, c)^T$ , and  $f = \chi_2 \circ \chi_1$  with  $\chi_1$  being the linear map

$$\chi_1 I = \begin{pmatrix} \frac{1}{2} & 0 & -\frac{1}{2} & 0 \\ 0 & -\frac{1}{2} & 0 & \frac{1}{2} \\ \frac{1}{4} & \frac{1}{4} & \frac{1}{4} & \frac{1}{4} \end{pmatrix} I, \quad (15)$$

and

$$\chi_2(x, y, c) = [\Phi^{-1}(x, y), c]^T, \quad (16)$$

where  $\Phi$  is the polar coordinates map  $\Phi(A, \phi) = [A \cos(\phi), A \sin(\phi)]$ .

The Jacobian of  $f$  can be calculated via the usual differentiation rules  $D(\Phi^{-1})[\Phi(A, \phi)] = [D\Phi(A, \phi)]^{-1}$  and  $Df(I) = D\chi_2(\chi_1(I)) \cdot D\chi_1(I) = D\chi_2(\chi_1 I) \cdot \chi_1 I$ , which finally leads to

<sup>8</sup>For example, if one measures the length  $x$  of one side of a “perfect” square with an error  $\sigma$ , the bias for computing the area  $A$  of that square by assuming  $A = \langle x \rangle^2$  is  $\langle x^2 \rangle - \langle x \rangle^2 = \text{Var}(x) = \sigma^2$ .

<sup>11</sup>See Ref. 27. Note that therein the factor  $1/2$  is missing.



$$Df(j) = \frac{1}{2} \begin{pmatrix} \cos(\phi) & -\sin(\phi) & -\cos(\phi) & \sin(\phi) \\ -\frac{1}{A} \sin(\phi) & -\frac{1}{A} \cos(\phi) & \frac{1}{A} \sin(\phi) & \frac{1}{A} \cos(\phi) \\ \frac{1}{2} & \frac{1}{2} & \frac{1}{2} & \frac{1}{2} \end{pmatrix}, \quad (17)$$

with  $j$  being some point in the preimage of  $(A, \phi, c)^T$ , which will be omitted from now on. Also, we will no longer distinguish estimators/measurements notationally from “real” values.

Now assume the simple case where the measurements of the  $I_n$ 's are independent and identically distributed, such that  $\text{Var}(I) = \text{diag}(\sigma^2, \dots, \sigma^2)$  for some error  $\sigma$ . In this case, one computes

$$\begin{aligned} \text{Var}(A, \phi, c) &= Df \text{Var}(I) Df^T = Df Df^T \sigma^2 \\ &= \text{diag}\left(\frac{1}{2}, \frac{1}{2A^2}, \frac{1}{4}\right) \sigma^2, \end{aligned} \quad (18)$$

or explicitly,

$$\text{Var}(A) = \frac{\sigma^2}{4}, \quad \text{Var}(\phi) = \frac{\sigma^2}{2A^2}, \quad \text{Var}(c) = \frac{\sigma^2}{2}. \quad (19)$$

#### 4.2 Phase Probability Distribution

The variance of the phase can also be obtained directly by transforming the probability distributions of the raw values to the distribution of the phase. The resulting spread shows the same behavior as with the first order approximate error propagation in Sec. 4.1. Here we derive that the phase  $\phi_d$  calculated with the four-phase algorithm [Eqs. (22) and (23)] follows an offset normal distribution. The derivation shows how its variance relates to given variances  $\sigma_n^{\text{raw}}$  of the raw signals  $I_n$  for phase calculations in four channel mode and eight channel mode, respectively. Additionally we take into account here that each pixel on the chip physically has two different gates  $A$  and  $B$ , where the reference signal at gate  $B$  is shifted by  $\pi$  with respect to the signal at gate  $A$ :  $A_n = I_n$ ;  $B_n = I_{n+2}$ . In the preceding derivation, this was neglected by assuming equal variances of the raw values. Here, we consider that the gates may have different variances  $\sigma_A$  and  $\sigma_B$ .

Assuming a harmonically modulated reference signal, the raw values are

$$I_n = c_{\text{phys}} + A_{\text{phys}} \cos(\phi_d + \alpha_n). \quad (20)$$

They are<sup>16</sup> shifted by the angles  $\alpha_n = (2\pi n)/N$ ,  $n = 0, \dots, N-1$

$$\Rightarrow A_n - B_n = 2A_{\text{phys}} \cos(\phi_d). \quad (21)$$

Here,  $A_{\text{phys}}$  is the amplitude of the physical signal, which we will distinguish from the amplitude  $A$  of the computed signal in the later equations. The phase can be computed from the raw signals with

$$\phi_d = \arg(\text{Re} + i \text{Im}), \quad (22)$$

where

$$\begin{aligned} \text{Im} &= \begin{cases} B_1 - A_1 & \text{four channels} \\ A_3 - B_3 + B_1 - A_1 & \text{eight channels} \end{cases} \\ \text{Re} &= \begin{cases} A_0 - B_0 & \text{four channels} \\ A_0 - B_0 + B_2 - A_2 & \text{eight channels.} \end{cases} \end{aligned} \quad (23)$$

Thus, in principle, one needs to acquire only two raw values at each gate, respectively. The eight-channel mode is used for two reasons. One advantage is that the amplitude of the modulation signal is doubled, which leads to a smaller variance as shown by the following derivation. The other reason is that it is robust to unequal sensitivities of the two different gates at each pixel. We will deal with this in Sec. 4.3.1.

The recording of electrons in the two gates  $A$  and  $B$  corresponds to a Poisson process. In the limit of many accumulated charges (that is, with reasonable exposure time), the values of the raw channels are normally distributed with  $\sigma_A$  and  $\sigma_B$ , where  $\sigma_{\text{raw}} := [(\sigma_A^2 + \sigma_B^2)/2]^{1/2}$ . Since  $\text{Im}$  and  $\text{Re}$  are the sum of an equal number of raw signals from gate  $A$  and gate  $B$ , respectively [Eq. (23)] we have [with Eq. (21)] that  $A = (\mu^2 + \nu^2)^{1/2} := (\langle \text{Im} \rangle^2 + \langle \text{Re} \rangle^2)^{1/2} = 2A_{\text{phys}}$  for four channels ( $A = 4A_{\text{phys}}$  for eight channels) and  $\sigma := \sigma_{\text{Im}} = \sigma_{\text{Re}} = \sqrt{2}\sigma_{\text{raw}}$  for four channels ( $\sigma = 2\sigma_{\text{raw}}$  for eight channels).

Therefore the tuple  $\mathbf{x} = (\text{Im}, \text{Re})$  follows an isotropic bivariate Gaussian distribution with variance  $\sigma^2$  and mean  $(\mu, \nu)$ :

$$\begin{aligned} G(\vec{x}; \mu, \nu, \sigma) dx dy &= \frac{1}{2\pi\sigma^2} \exp\left\{-\frac{1}{2}\left[\frac{(x-\mu)^2 + (y-\nu)^2}{\sigma^2}\right]\right\} dx dy. \end{aligned} \quad (24)$$

Going to polar coordinates  $\mathbf{x} = r[\cos(\phi_d), \sin(\phi_d)]^T$ ,  $dx dy = r dr d\phi_d$ , we obtain

$$\begin{aligned} G_{\text{pol}}(r, \phi_d; \mu, \nu, \sigma) r dr d\phi_d &= \frac{r}{2\pi\sigma^2} \exp\left\{\frac{2r[\mu \cos(\phi_d) + \nu \sin(\phi_d)] - r^2 - \mu^2 - \nu^2}{2\sigma^2}\right\} dr d\phi_d \\ &= r G[(\mu, \nu)^T; 0, 0, \sigma] \exp\left\{-\frac{1}{2\sigma^2}[r^2 - 2ra(\phi_d)]\right\} dr d\phi_d, \end{aligned} \quad (25)$$

where  $a(\phi_d) = \mu \cos(\phi_d) + \nu \sin(\phi_d)$ .

The probability distribution of the angles is obtained by projecting  $G_{\text{pol}}(r, \phi_d; \mu, \nu, \sigma)$  on the unit circle (that is, by integrating out  $r$ ). In Fig. 1 (left) this is illustrated graphically. Using

$$\begin{aligned} \int_0^\infty r \exp\left[-\frac{p^2}{2}(r^2 - 2rq)\right] dr &= \frac{1}{p^2} \left\{ 1 + qp \left(\frac{\pi}{2}\right)^{1/2} \exp\left(\frac{q^2 p^2}{2}\right) \left[ 1 + \text{erf}\left(\frac{qp}{\sqrt{2}}\right) \right] \right\}, \end{aligned} \quad (26)$$

this leads to

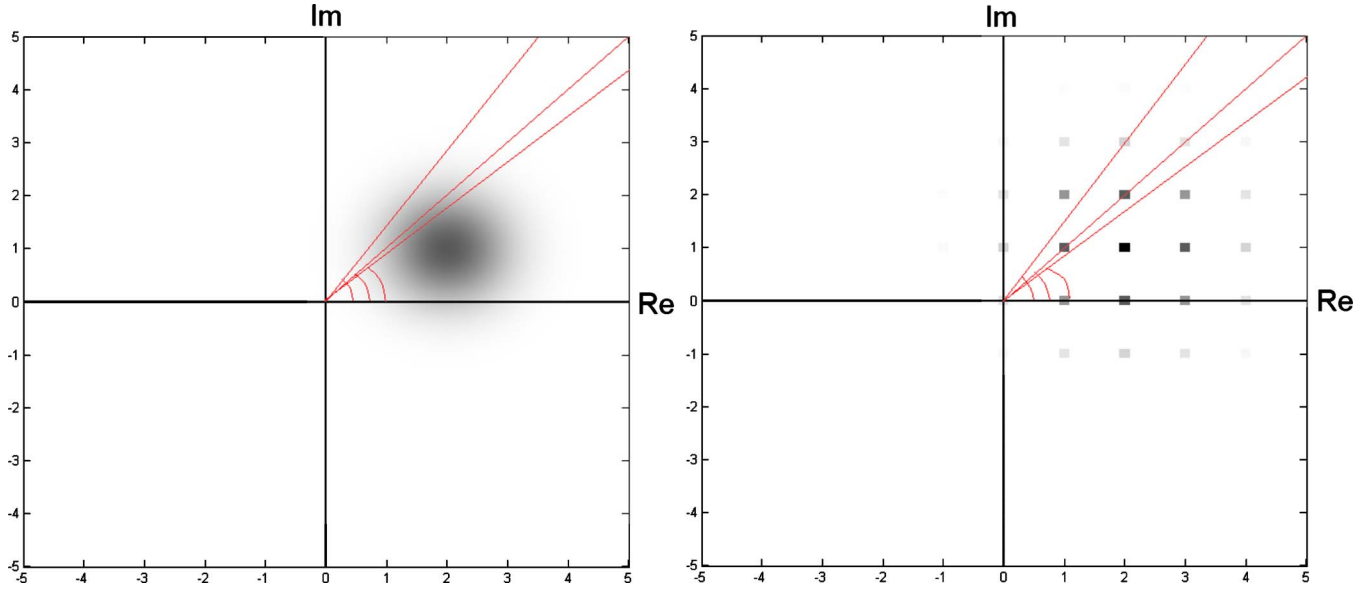


**Fig. 1** Genesis of the phase distribution. The raw intensities lead to an isotropic bivariate Gaussian in the complex plane. Points of equal phase lie on rays emanating from the origin (like the three red examples). Left: neglecting quantization, the phase distribution can be obtained by simply integrating over points of constant phase. Right: with quantized raw values different angles have different densities of allowed values, which leads to the characteristic shape of the resulting phase distributions (compare Fig. 6). (Color online only.)

$$\begin{aligned}
 G_c(\phi_d; \mu, \nu, \sigma) &= \int_0^\infty G_{\text{pol}}(r, \phi_d; \mu, \nu, \sigma) r dr \\
 &= \sigma^2 G[(\mu, \nu)^T; 0, 0, \sigma] \left( 1 + \left( \frac{\pi}{2} \right)^{1/2} \frac{a(\phi_d)}{\sigma} \right. \\
 &\quad \left. \times \exp \left[ \frac{a(\phi_d)^2}{2\sigma^2} \right] \left\{ 1 + \operatorname{erf} \left[ \frac{a(\phi_d)}{\sqrt{2}\sigma} \right] \right\} \right). \quad (27)
 \end{aligned}$$

Since  $G_c(\phi_d; \mu, \nu, \sigma)$  is equivariant under rotations around the origin, we can consider the case  $\nu=0 \Rightarrow \mu=A$  without loss of generality. The general case can then be expressed by simply rotating the basis [that is, by substituting  $\phi_d$  with  $(\phi_d - \bar{\phi}_d)$ ]. However, to keep equations short we set  $\bar{\phi}_d=0$ . With having  $\nu$  and  $\mu$  fixed, we will denote the distribution in the following as  $G_c(\phi_d; A/\sigma)$ :

$$\begin{aligned}
 G_c(\phi_d; A/\sigma) &:= G_c(\phi_d; A, 0, \sigma) \\
 &= \frac{1}{2\pi} \exp \left( \frac{-A^2}{2\sigma^2} \right) \left( 1 + \left( \frac{\pi}{2} \right)^{1/2} \frac{A}{\sigma} \cos(\phi_d) \right. \\
 &\quad \left. \times \exp \left[ \frac{A^2 \cos^2(\phi_d)}{2\sigma^2} \right] \left\{ 1 + \operatorname{erf} \left[ \frac{A \cos(\phi_d)}{\sqrt{2}\sigma} \right] \right\} \right). \quad (28)
 \end{aligned}$$

This is a specific instance of the offset normal distribution (see Fig. 2). Now that the probability distribution of the phase is known, its exact variance  $\operatorname{Var}(\phi_d) = \int_{-\pi}^{\pi} \phi^2 G_c(\phi_d; A/\sigma) d\phi$  can be numerically computed. Doing this, we found that it is feasible to approximate it as the reduced spread parameter  $\sigma_{\text{red}} := \sigma/A$  for reasonable  $\sigma/A$ .

In this formulation, it is intuitive to see that the variance of the phase strongly depends on the physical modulation amplitude  $A_{\text{phys}}$  of the modulation.

$$\operatorname{Var}(\phi_d) \approx \sigma_{\text{red}}^2 = \begin{cases} \frac{\sigma_{\text{raw}}^2}{2A_{\text{phys}}^2} & \text{four channels} \\ \frac{\sigma_{\text{raw}}^2}{4A_{\text{phys}}^2} & \text{eight channels.} \end{cases} \quad (29)$$

Without much effort, one finds that the limit behavior of  $G_c(\phi_d; A/\sigma)$  with respect to the reduced amplitude  $A_{\text{red}} = A/\sigma$  is

$$\lim_{A_{\text{red}} \rightarrow 0} G_c(\phi_d; A_{\text{red}}) = \frac{1}{2\pi}, \quad (30)$$

$$\lim_{A_{\text{red}} \rightarrow \infty} G_c(\phi_d; A_{\text{red}}) = \delta(\phi_d - \bar{\phi}_d). \quad (31)$$

In practice, both limiting cases cannot be observed directly in the range distributions due to two effects. In the case of high amplitudes, the PMD sensor shows saturation effects and delivers extremely noisy and strongly biased signals. At low amplitudes, the quantization of the raw signals soon leads to a population of only a small number of phases. Figure 11 in Sec. 5.4 illustrates these two effects with measured data.

Since the mathematical form of the projected normal distribution may seem inconvenient for some applications, one may prefer to use a simpler probability distribution that does not differ much in shape. Note for this purpose that the shape of the projected normal distribution is very close

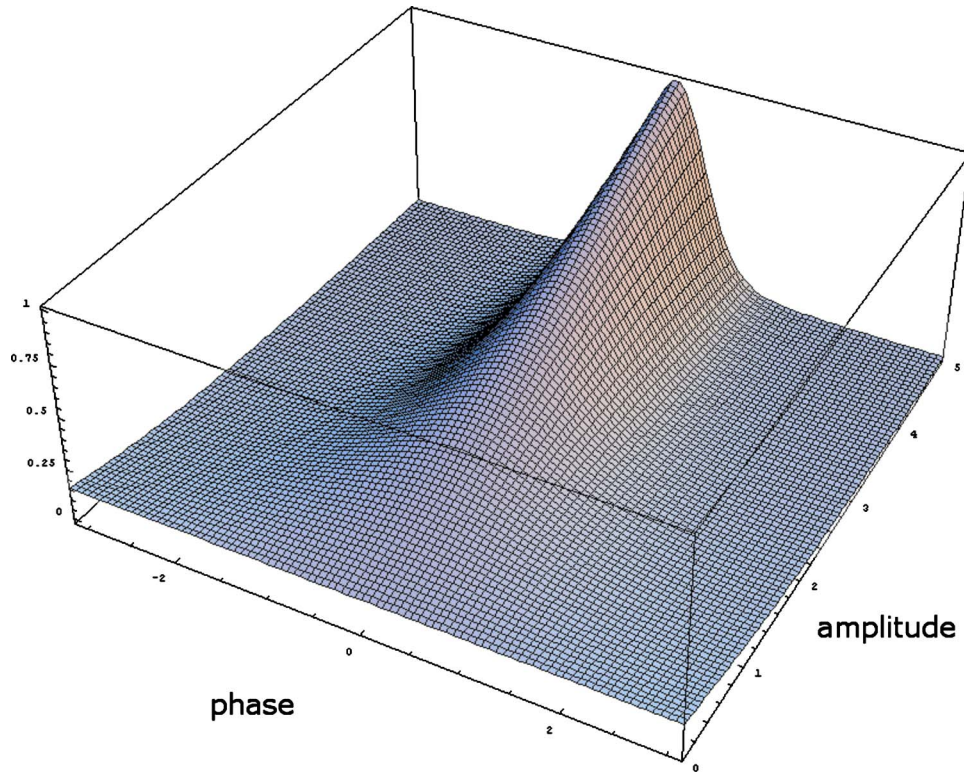


**Fig. 2** Probability distribution of the phase as a function of the modulation amplitude. Neglecting quantization effects, the phase follows an offset normal distribution (see text) that converges to the uniform distribution in the limit of low amplitudes.

to that of the von Mises distribution which is typically used in the context of circular data.<sup>28</sup> Whereas the offset normal distribution is derived by projecting an isotropic bivariate Gaussian onto the unit circle the genesis of the von Mises distribution is slightly different. Here the probabilities on the unit circle are cut out of the Gaussian and are then renormalized by Bessel functions. Or in shorter terms, given a bivariate Gaussian distribution  $G(\phi, r)$ , the offset Gaussian is the marginal  $G(\phi)$  and the von Mises is the renormalized conditional distribution  $G(\phi|r=1)$ . The spread parameter  $\kappa$  of the latter corresponds<sup>28</sup> to  $1/[\text{Var}(\phi_d)]$ .

### 4.3 Numerical Computation of the Quantization Error

After data acquisition, the analog raw signals  $I_n$  are converted to digital numbers before the phase  $\phi_d$  is computed as in Eqs. (23) and (22). The rounding errors due to conversion propagate through the calculation and finally lead to errors in phase. Here, we show numerically the extent of the resulting error. It turns out that it does not depend only on the resolution of the analog-digital conversion but also on the amplitude and even on the phase itself. In addition, we show that at a given amplitude  $A_{\text{phys}}$  only a few different phase values can be populated. This explains the frequent occurrence of only a few several depth values  $d$  at low amplitude as one can observe in the data (see for instance Fig. 3). In our first numerical calculation, we compute the resulting quantization bias of  $\phi_d$  as a function of

$A_{\text{phys}}$  and  $\phi_{\text{real}}$  for noiseless raw signals. Then the discrete probability distribution of  $\phi_d$  is computed for several amplitudes given noisy raw signals.

#### 4.3.1 Impact of quantization on the range bias

Neglecting noise in the raw signals, the result of the phase calculation for a given phase  $\phi$  and amplitude  $A_{\text{phys}}$  with harmonically modulated reference signal can be simulated numerically. Again we assume a harmonically modulated reference signal such that the raw values are  $I_n = c_{\text{phys}} + A_{\text{phys}} \cos(\phi + \alpha_n)$  and shifted by the angles  $\alpha_n = (2\pi n)/N$ ;  $n=0, \dots, N-1$ . Thereby, the  $I_n$  comes from the two different gates A and B (shifted with  $\pi$ ) that are subject to different pixel dependent systematic errors due to different sensitivities  $a_i$  and  $b_i$ :

$$A_n = a_1 I_n + a_0, \quad B_n = b_1 I_{n+2} + b_0. \quad (32)$$

The advantage of the eight-channel mode is that the fixed pattern noise due to different sensitivities of the gates cancel in Im/Re, as shown by Ref. 26 [one can see this by substituting the  $A_n$ s and  $B_n$ s in Eq. (23)]. Values of the signal offset  $c_{\text{phys}}$  are usually between 2000 and 4000 in arbitrary units for the PMD[vision]® 19k camera system. Using these units, the quantization is performed with accuracy 1, i.e., the  $I_n$  are rounded to integers. All further calculations will use these arbitrary units. Taking this quantization into account the raw values at channel A and B are now

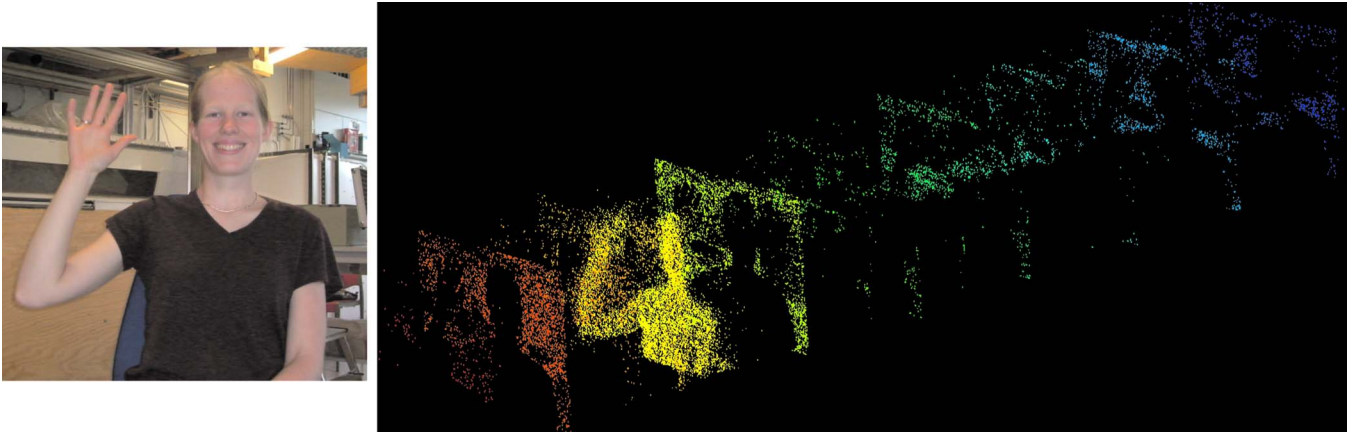


**Fig. 3** Indoor scene as observed by a conventional digital camera and by a 3-D camera system at 5-ms exposure time. The output is displayed by the software CamVisPro. The spurious “walls” at discrete depths are artifacts produced by pixels with low amplitude, see Sec. 4.3.2.

$$A_n = \text{round}\{a_1[c_{\text{phys}} + A_{\text{phys}} \cos(\phi + \alpha_n)] + a_0\},$$

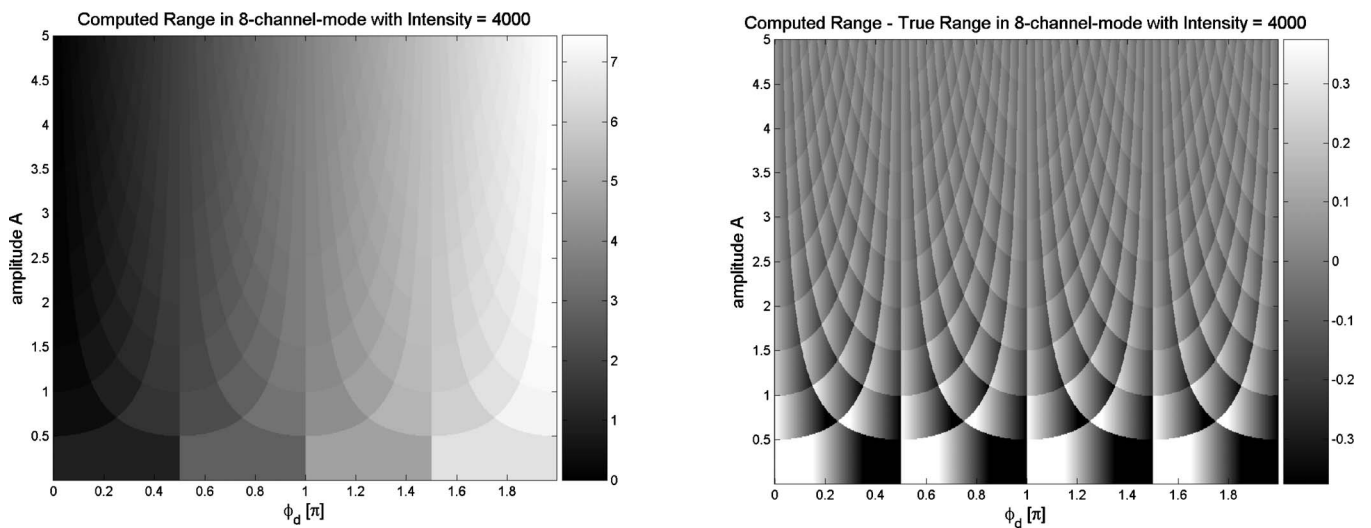
$$B_n = \text{round}\{b_1[c_{\text{phys}} + A_{\text{phys}} \cos(\phi + \alpha_{n+2})] + b_0\}. \quad (33)$$

The phase can again be computed from the raw signals via the four phase algorithm Eqs. (22) and (23). Thereby, one needs to keep the information about which quadrant the vector  $(\text{Im}, \text{Re})^T$  lies in.

In Fig. 4, the resulting phase  $\phi_d$  was computed for small amplitudes and for phases  $0 \leq \phi_d < 2\pi$ , which corresponds to all possible ranges from 0 to 7.5 m. To give an idea of the range bias, we have plotted the resulting range  $d$  computed from its relation to the phase delay  $\phi_d = (4\pi f/c)d$ , where  $c$  is the speed of light, and  $f$  is the modulation frequency of the diodes and the reference signal. The plot illustrates very well the poor range resolution at vanishing amplitude due to quantization. Since only a few phase val-

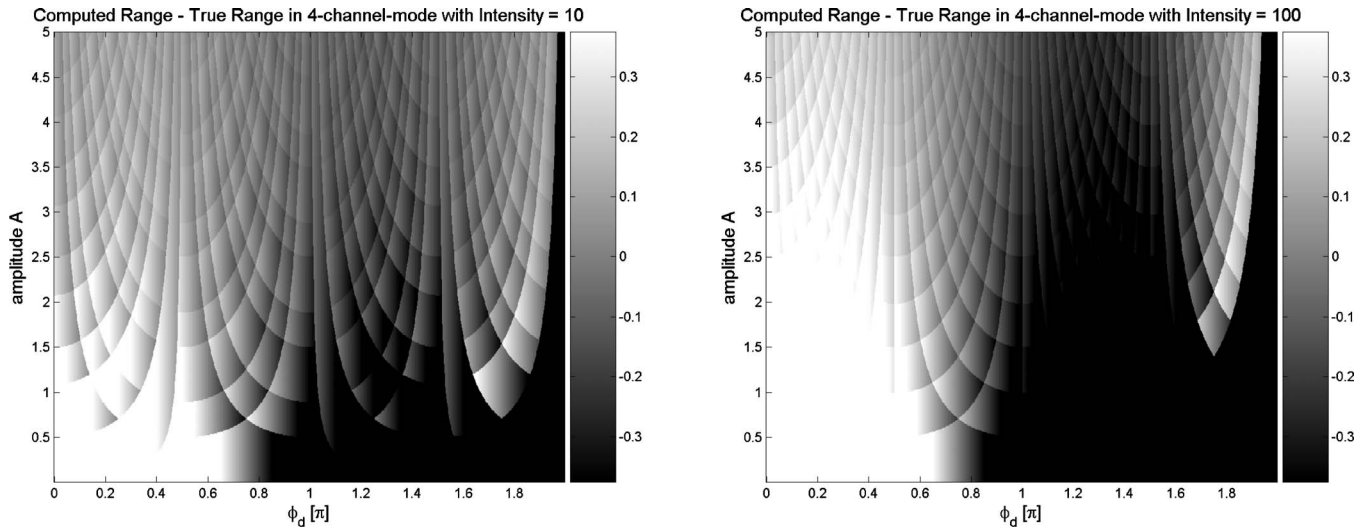
ues can be populated at a given low  $A_{\text{phys}}$ , the bias depends on the phase itself and decreases as  $A_{\text{phys}}$  rises. To keep this visible for all amplitudes up to 5, color scale in Fig. 4 (right) has been truncated to a maximum bias of 40 cm. Note that this makes absolute values higher than 40 cm as for amplitudes  $< 1$  invisible.

Figure 5 shows two plots of the bias for ranges computed in the four channel mode. Two different signal intensities  $c_{\text{phys}}$  were used. In all calculations we used a small linear difference in sensitivity between gates A and B of about 1%. In the eight-channel mode this deviation is canceled as predicted by Ref. 26 and therefore has no impact on the quantization error. But regarding Fig. 5, it is obvious that sampling only two phases from gate A and B, respectively, would lead to strong systematic errors. This is one reason why—even if not necessary in theory—each gate has to acquire four raw values, each at a different time. The



**Fig. 4** Range numerically computed from eight raw channels (left) and the bias (right) in units of meters. The bias is due to quantization of the eight raw values. The computation of the range amplifies this rounding error especially at low amplitudes. In this regime, only a few range values can be occupied. It is evident that the bias does not only depend on the modulation amplitude but also on the range itself.





**Fig. 5** Bias of the expected range for a constant intensity offset of 10 (left) and 100 (right). Given a difference in the sensitivity between gate A and B of about 1% the four-channel calculation produces systematic errors depending strongly on the overall intensity. The same color scale as in Fig. 4 (right) was used for the sake of comparability. (Color online only.)

other reason is that taking more raw values amplifies the physical modulation amplitude  $A_{\text{phys}}$  of the signal and thus reduces the variance of the computed range (see Sec. 4.2).

#### 4.3.2 Impact of quantization on the phase probability distribution

After calculating the impact of quantization on the range bias with noiseless raw data in the previous section, we now focus on the probability distribution of the resulting range under noisy input. The raw channels  $A_n$  and  $B_n$  follow Gaussian distributions with standard deviations  $\sigma_A^{\text{raw}}$  and  $\sigma_B^{\text{raw}}$ . Quantization of these values leads to discrete distributions. We chose the same dimensioning of the values  $A_{\text{phys}}$  and  $c_{\text{phys}}$ , as in the last section and set  $\bar{\phi} = \pi$  and  $\sigma_A^{\text{raw}} = \sigma_B^{\text{raw}} = 1$  to compute these distributions.<sup>¶</sup> In eight-channel mode [Eq. (23)], two raw values of each gate A and B are added for Im and Re, respectively. This leads to a discrete bivariate distribution in the plane with same width in  $x$  and  $y$  directions. Taking now the phases according to Eq. (22) and summing up all values resulting in the same phase finally gives the probability distribution of  $\phi_d$ , as shown in Fig. 6 for several amplitudes  $A_{\text{phys}}$ .

This discrete distribution substitutes the offset normal distribution that would be obtained without quantization (Sec. 4.2). How to characterize this distribution? The spread of a set of directional data can be expressed via the mean resultant length<sup>28</sup> (MRL). MRL takes values between 0 and 1, where 0 corresponds to maximal scattered angles and 1 to 0 variance. We have used this measure to illustrate the spread of the expected distributions (see Fig. 7). As expected it converges to 1 with rising amplitude. However, the variation also depends on the phase because the quantization lattice is not isotropic.

<sup>¶</sup>It would make no difference if  $\sigma_A^{\text{raw}} \neq \sigma_B^{\text{raw}}$ , since the raw values  $I_n$  are added as in Eq. (23) bottom.

## 5 Experiments

To verify the theoretically derived error sources we performed measurements with the prototype camera PMD 19k from PMDtec (see Table 1 for specification). This particular camera was chosen because internal digital postprocessing can be bypassed by direct readout of the raw intensities, thus enabling a direct investigation of the intrinsic errors of the measurement concept. These errors are representative for other prototypes using continuous-wave correlation. The following experiments are restricted to illustrating the errors derived in the earlier chapters. We do not consider effects that are unique for particular realizations of the measurement principle. This also includes the angular resolution, which strongly depends on the number of pixels that a camera has (there are sensors that measure only one value up to systems with  $1000 \times 1000$  pixels).

As a target, a checkerboard composed of patches with four defined reflectivities of 84, 50, 25, and 12.5% was installed on a moving stage with millimeter precision. The range, amplitude and raw values from the PMD 19k camera were acquired at equispaced displacements of the moving target using integration times from 0.1 to 30 ms. The target was oriented perpendicular to the optical axis in all our experiments.

The moving stage can be positioned precisely, but the distance between the camera lens and the closest point of the target cannot be used as a ground truth for the whole target since the camera measures the radial distance and not the Cartesian  $z$  coordinate. A pinhole model was used to determine, for each position of the moving stage, where on the image the target should be located and at what depth. In addition, this approach has allowed to concentrate on particular patches of the checkerboard in order to investigate the influence of the reflectivity. The next sections detail the geometrical model and the results of the measurements.

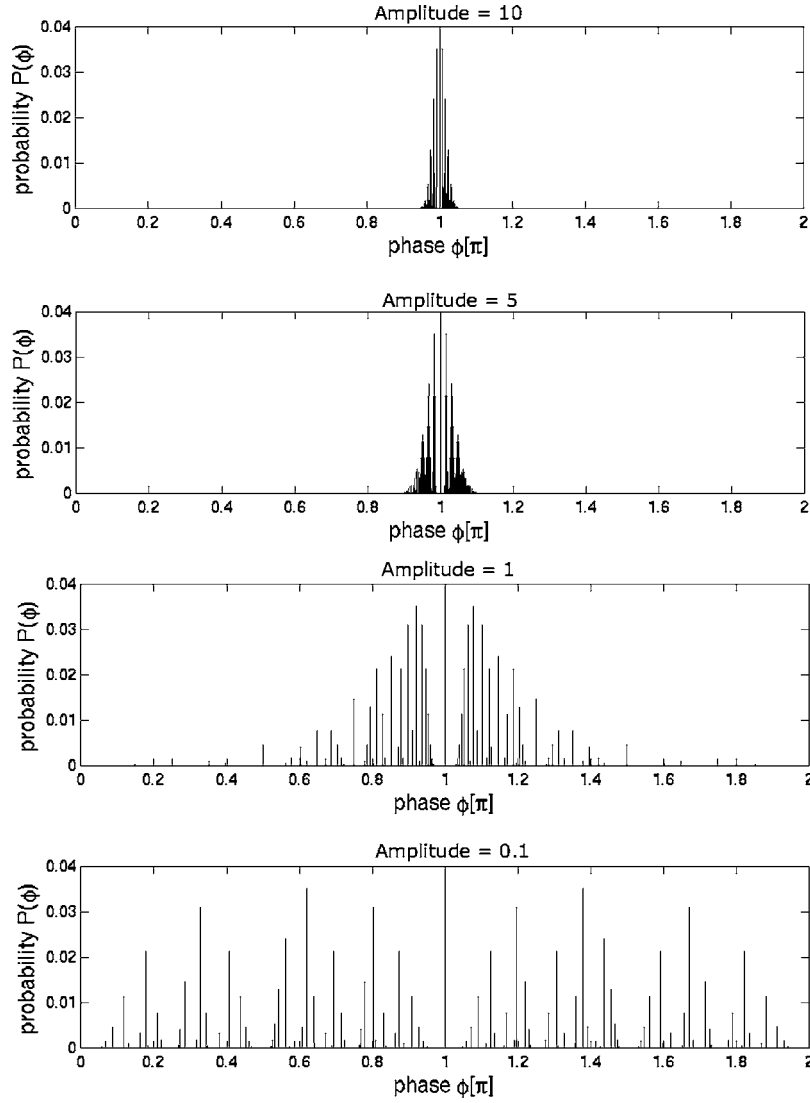


**Fig. 6** Probability distribution of  $\phi_d$  calculated from eight Gaussian distributed raw values  $I_n$  for various amplitudes  $A$ . Due to rounding of the raw values, their differences can only be located at certain points in the complex plane [compare Fig. 1 (right)]. Summing over the corresponding angles (the phase) leads to these characteristic distributions. At high amplitudes the angles can be better resolved whereas at low amplitudes the phases are only sparsely populated.

### 5.1 Geometrical Model

A simple pinhole model was used to map the depth image on the ground truth and thus allow for quantitative characterization of the camera. Here the conversion from Cartesian world coordinates  $(x, y, z)$  to the chip coordinates  $(m', n', r)$  is

$$m' = \text{round}\left(\frac{f}{p_d} \frac{y}{z}\right),$$

$$n' = \text{round}\left(\frac{f}{p_d} \frac{x}{z}\right),$$

$$r = (x^2 + y^2 + z^2)^{1/2}, \quad (34)$$

where  $p_d$  is the physical size of one pixel on the chip, and  $f$  is the focal length. The origin of the chip coordinates was chosen to be on the center of the chip and the origin of the world coordinates is in the lens (the pinhole). The  $z$  axis is the optical axis. Since the camera delivers the radial distances  $r$ , the inverse conversion is trivial. A flat patch, described with normal vector  $\mathbf{n}$  and space point  $\mathbf{x}_0$ , can be transformed from world coordinates to chip coordinates:

1. Transform the vertices of the object to chip coordinates.
2. Check which pixels are inside the resulting polygon.
3. For each of these pixels, compute the intersection of

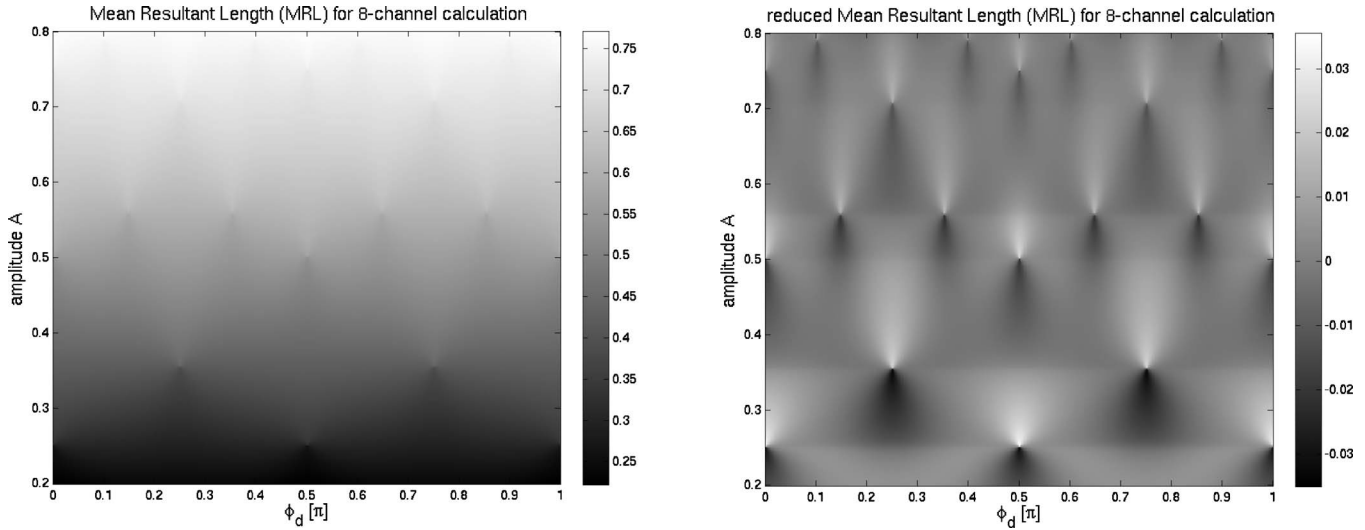


**Fig. 7** MRL of simulated phase distributions (like those shown in Fig. 6) at given amplitude  $A$  and mean phase  $\phi_d$  obtained from eight raw intensities (top). Bottom: Since the complex plane is not isotropic once the raw values are quantized, the MRL does not depend only on the amplitude but also slightly on the phase itself. This is underlined by subtracting the overall trend of MRL with respect to the amplitude. In the interval from  $\pi$  to  $2\pi$  the patterns merely repeat periodically.

the object and a ray emanating from the center of the pixel.

4. Transform the coordinates of the point of intersection to chip coordinates.

The third and the fourth step can be performed at the same time by noting that for an arbitrary point  $\mathbf{x}$  on the surface

$$\mathbf{x} = \frac{r}{[(p_d n')^2 + (p_d m')^2 + f^2]^{1/2}} (-p_d n', -p_d m', f)^T, \quad (35)$$

it holds that

$$\mathbf{n} \cdot (\mathbf{x} - \mathbf{x}_0) = 0 \Rightarrow r = \frac{\mathbf{n} \cdot \mathbf{x}_0 [(p_d n')^2 + (p_d m')^2 + f^2]^{1/2}}{n_x f - n_x p_d n' - n_y p_d m'}, \quad (36)$$

where  $n'$  and  $m'$  are distances from the center of the chip in pixel units.

## 5.2 Amplitude Behavior

For a characterization of the camera the amplitude of the sinusoidal modulation signal from Eq. (7) is at least as important as the range information itself since it sheds light on the reliability of the latter. The amplitude obviously depends on the integration time and on the reflectivity of the object, but also on the distance itself, see Fig. 8. This figure shows the amplitude observed from a patch of 84% reflectivity for various integration times. For higher reflectivities, the curves are merely shifted to the right. The amplitude drops rapidly with distance. For longer distances and for the integration times shown here, the signal can no longer be used. We used exposure times up to 30 ms to acquire reliable data for the whole range. However, at higher integration times a saturation effect is observed that masks the modulation amplitude. Figure 8 shows the sharp drop from the maximum to a low value and a further slow decrease toward zero (see markers *A* and *B*). Considering that the amplitude is computed from a difference of two or four raw values, one can interpret the fast drop as the region where one raw value is already saturated and the other one is approaching saturation. Once they are both saturated, their difference, and hence the estimated amplitude, becomes zero. The consequences will be discussed in the next section.

Since the variance of the estimated distance strongly depends on the amplitude, a higher dynamic range of the sensor would be desirable. Future systems will possibly make use of stronger light sources such as vertical lasers<sup>29</sup> and employ sensors with logarithmic behavior.<sup>30</sup>

**Table 1** PMD 19k datasheet.

Pixel dimensions	40 × 40 $\mu\text{m}$
Resolution	160 × 120
Optical fill factor	30%
Modulation frequency	20 MHz
Max. field of view	40 deg
Focal length	12 mm
Illumination power	≈ 3 W optical
Wavelength	870 nm
Frame rate	up to 15 fps
Analog-to-digital converter	12 bits

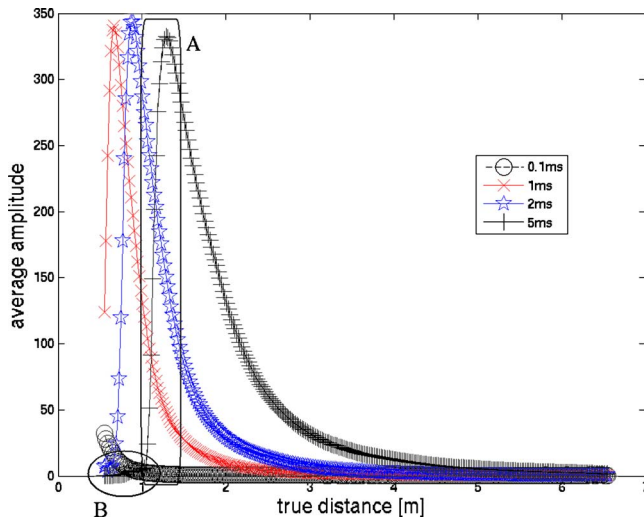


**Fig. 8** Average amplitudes for various integration times. The data was acquired from a patch with 84% reflectivity. The amplitude decreases fast with the distance. At very low distances the amplitude drops to a low value (A) and further slowly decreases toward zero (B) due to saturation effects. Curves of higher integration times or higher reflectivities are merely shifted to the right.

### 5.3 Depth Bias and Variance

Every particular camera has its specific constant bias due to a delay between the reference signal at the diodes and on the chip itself. We have determined this offset once and then corrected for it in all further measurements. All figures show corrected values.

In addition to this constant bias, there is a sinusoidal bias in the magnitude of about 5 cm as can be seen in Fig. 9 (right). The suspected cause is an imperfect shape of the reference signal: the phase calculation assumes a sinusoidal reference signal, but the actual reference signal has rather a rectangular shape. Numerical simulations show that the

systematic error due to this wrong assumption leads to a sinusoidally shaped bias.<sup>11,16,26</sup> Given the exact waveform of the reference signal, the calculation of the phase could be adapted to avoid this effect, as discussed in Sec. 3.2. The alternative approach is to tabulate the residuals and correct for them as shown for instance in Ref. 21.

At longer distances, one can observe a large deviation from the true range for short integration times (Fig. 9, left). Although the deviation may look like another form of bias in this plot, it is in fact the consequence of a large variance: For short integration times, the signal starts to become too small at long distances. Neglecting quantization effects, it can be shown that the estimated phase then follows a uniform distribution (Sec. 4.2). The estimated distance then occupies values in the whole unambiguous range. Since Fig. 9 shows the mean of all frames and pixels of a patch for every position, the resulting value converges to the middle of the unambiguous range with vanishing signal amplitude. Note that for the highest reflectivity (84%), all measurements with less than 5 ms integration time show this effect.

For short distances, there is another remarkable deviation (Fig. 9 at C). It occurs at different positions for higher integration times and is a consequence of a saturation effect (Fig. 11 in Sec. 5.4 bottom). The curves have the same shape but are shifted by the distance at which overexposure first occurs for each integration time. As discussed, the estimated mean depth then converges to the center of the unambiguous measurement interval. Again, the resulting deviation of the mean value from the ground truth is due to a high variance that can be observed if the depth values are not averaged before plotting (Fig. 11 in Sec. 5.4).

A method to mask overexposed pixels was proposed in Ref. 22 and enables us to observe an additional bias at very close distances that can be explained by the fact that the light source can no longer be considered as a point source in this region.

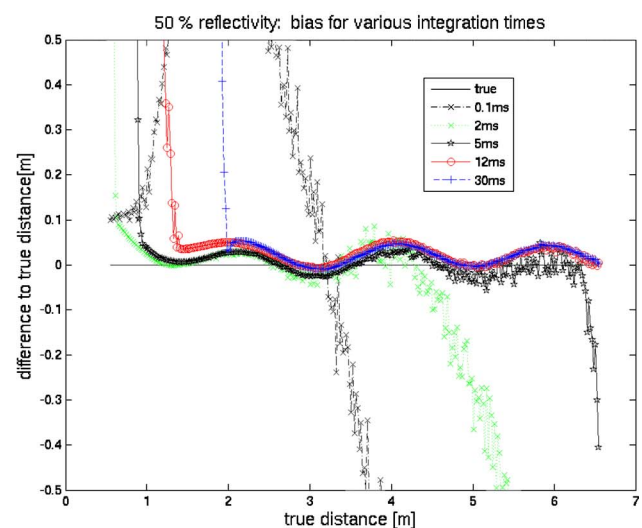
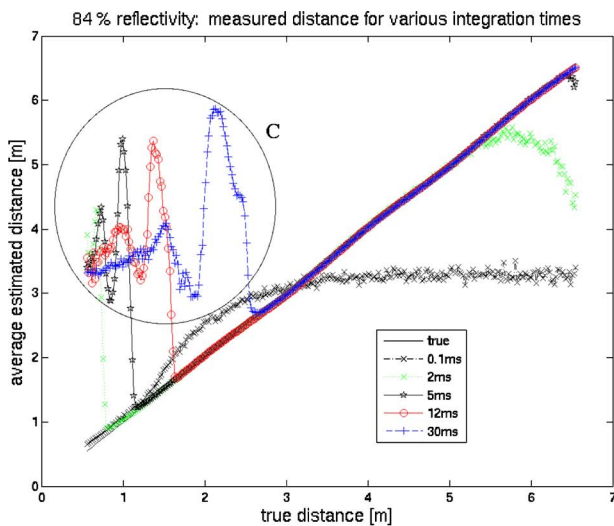


**Fig. 9** Average measured distance versus true distance (left) and bias versus true distance (right) for various integration times. The values are the average of 100 frames. Values were obtained from patches with 84% reflectivity (left) and 50% reflectivity (right), respectively. In both graphs the effect of low modulation amplitude as well as overexposure (C) can be observed. See text for discussion.



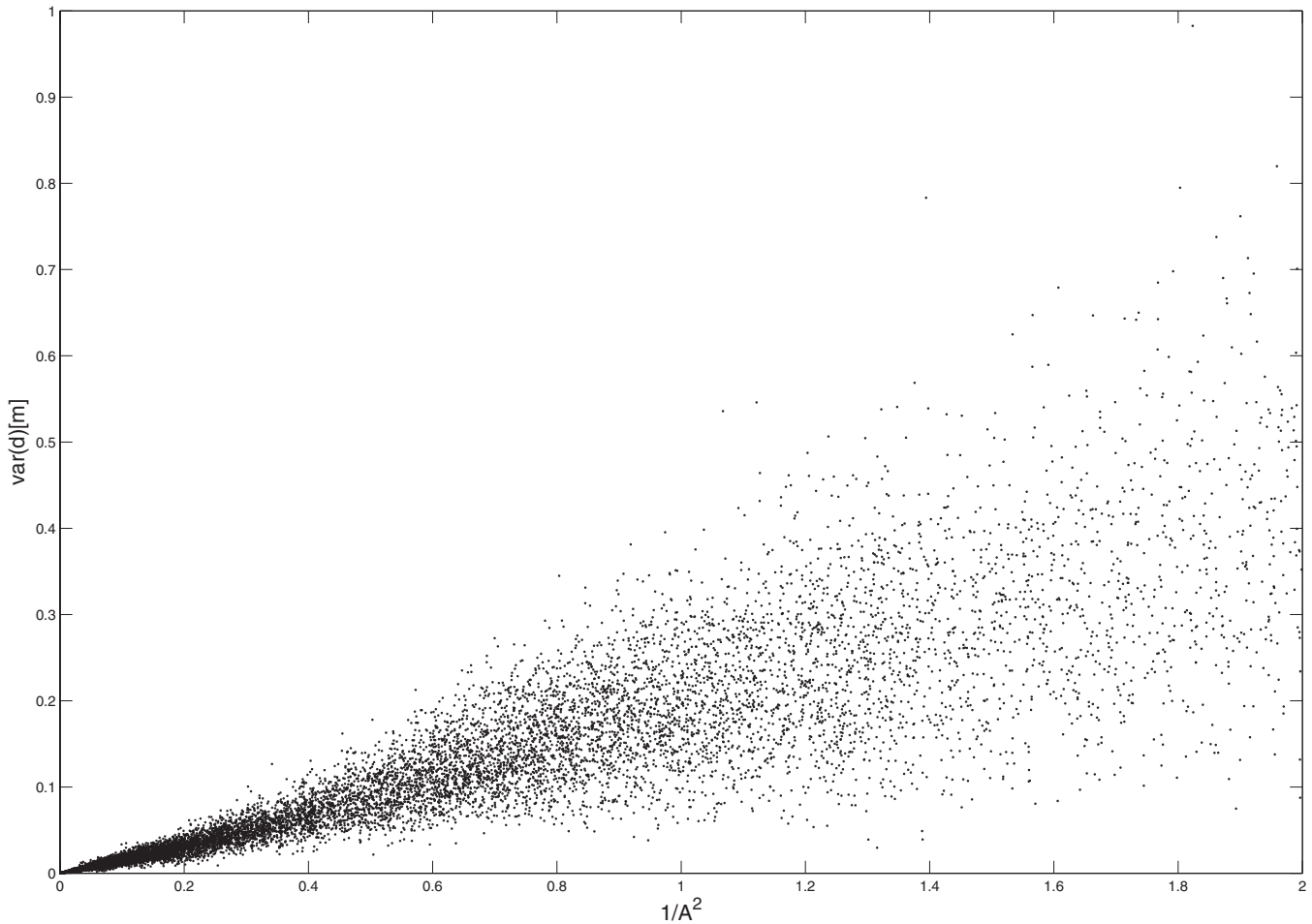


**Fig. 10** Temporal variance against  $1/A^2$  computed from a static scene. The figure corroborates the theoretical relation [Eq. (29)] derived in Sec. 4.2.

The  $1/A^2$  law relating variance to amplitude can be verified by recording an arbitrary static scene and plotting the temporal variance of each pixel against its value of  $1/A^2$  (Fig. 10).

#### 5.4 Quantization Error

In all results just discussed, the measured raw values were averaged over many frames to be able to observe systematic errors independently of noise. By averaging the information, though, the quantization errors vanish. Therefore, the results from single frames are presented in Fig. 11. Again, reflectivities of 84, 50, 25, and 12.5% were used with integration times ranging from 0.1 to 30 ms. Figure 11 shows the resulting curves for the target with 25% reflectivity. The amplitude curves for the other reflectivities are shifted to the left or to the right, but have the same shape. At first glance one can see the sparsity of the measured distances at low modulation amplitudes which are either due to weak signal (long distances) or saturation (short distances). For small amplitudes, the depth can assume only specific values (see Sec. 4.3) that are spread over the whole unambiguous range. Taking the mean would result in a distance value somewhere in the middle of the range as can be seen in Fig. 9 (left).

## 6 Conclusion and Outlook

We investigated the continuous-wave modulated TOF measurement principle and its associated errors for 3-D cameras. The mathematics of the required phase estimation has been derived in a concise fashion and we showed that the probability distribution of the resulting range is an offset normal distribution (also known as projected normal distribution). With this, the variance of the resulting distance estimate can be computed exactly and we have confirmed that  $\text{Var}(d) = 1/A^2$  is a good approximation. By modeling the measurement and estimation process, we showed that in the limit of low amplitudes, the depth map can exhibit very significant artifacts due to quantization. All theoretically derived error sources were illustrated by measurements. Other systematic errors such as the bias due to anharmonic signals and overexposure were discussed as well.

The errors addressed are intrinsic to this kind of 3-D camera, and even future models will suffer from low amplitudes due to large distances or low reflectivity. The noise in this regime could be reduced with adaptive integration times, which could also help avoid overexposure. Adaptive systems with two integration times already exist, and future cameras will perhaps be able to adapt continuously to the illumination conditions. The errors due to anharmonic sig-

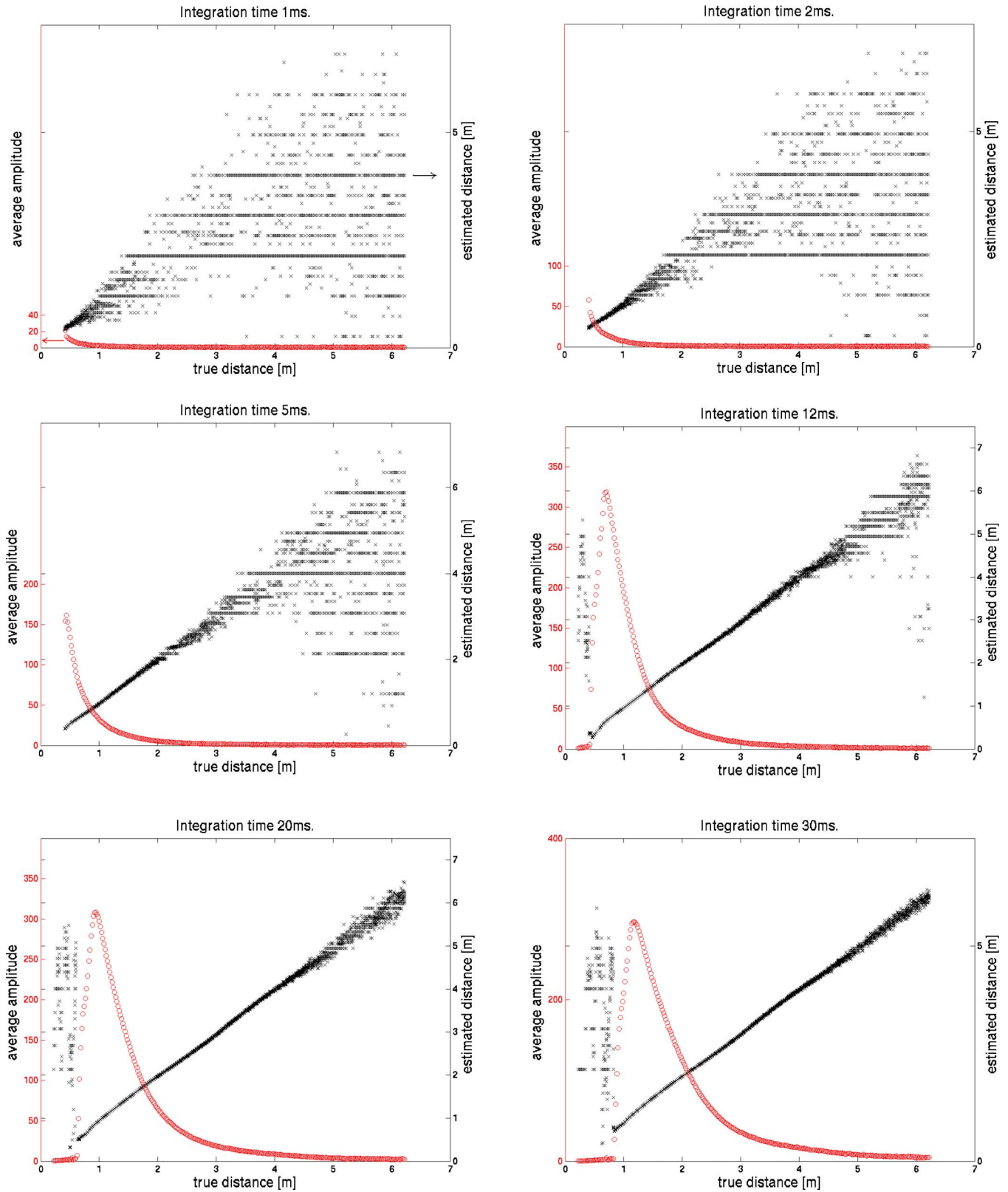


**Fig. 11** Estimated distances and average amplitude against true distance for various integration times and a target of 25% reflectivity. The quantization effect is clearly visible at the horizontal aligned measurement points and occurs both at overexposed pixels (left sides of bottom graphs) and at high distances (upper graphs). In both cases, the estimated amplitude of the sinusoid in Eq. (7) vanishes.

nals can be avoided by using appropriate calculations, provided the actual shape of the modulation signal is known. The quantization error could be drastically reduced if the raw values were quantized after the subtractions are carried out in analog. Of course this is a technical challenge and a physical realization could engender new error sources.

## References

1. R. A. Jarvis, "A laser time-of-flight range scanner for robotic vision," *IEEE Trans. Pattern Anal. Mach. Intell.* **5**, 505–512 (1983).
2. T. Spirig, P. Seitz, O. Vietze, and F. Heitger, "The lock-in CCD—Two-dimensional synchronous detection of light," *IEEE J. Quantum Electron.* **31**, 1705–1708 (1995).
3. R. Schwarte, H. G. Heinol, Z. Xu, and K. Hartmann, "A new active 3D-vision system based on rf-modulation interferometry of incoherent light," in *Photonics East—Intelligent Systems and Advanced Manufacturing, Proc. SPIE* **2588**, 12 (1995).
4. R. Lange, "3D time-of-flight distance measurement with custom solid-state image sensors in CMOS/CCD-technology," Dr.-Ing Diss., Department of Electrical Engineering and Computer Science, University of Siegen (2000); <http://deposit.dbb.de/cgi-bin/dokserv?idn=960293825>.
5. D. Nitzan, A. E. Brain, and R. O. Duda, "The measurement and use of registered reflectance and range data in scene analysis," *Proc. IEEE* **65**(2), 206–220 (1977).
6. W. T. Cathey and W. C. Davis, "Imaging system with range to each pixel," *J. Opt. Soc. Am. A* **3**(9), 1537–1542 (1986).
7. G. Beheim and K. Fritsch, "Range finding using frequency-modulated laser diode," *Appl. Opt.* **25**, 1439–1442 (1986).
8. P. Besl, "Active optical range imaging sensors," *Mach. Vision Appl.* **1**, 127–152 (1988).
9. C. Joenathan, "Phase-measuring interferometry: new methods and error analysis," *Appl. Opt.* **33**, 4147–4155 (1994).
10. T. Spirig, M. Marley, and P. Seitz, "The multitap lock-in CCD with offset subtraction," *IEEE Trans. Electron Devices* **44**(10), 1643–1647 (1997).
11. X. Luan, "Experimental investigation of the photonic mixer device and development of TOF 3D ranging systems based on PMD technology," Dr.-Ing Diss., Department of Electrical Engineering and Computer Science, University of Siegen (2001).
12. S. B. Gokturk, H. Yalcin, and C. Bamji, "A time-of-flight depth sensor—system description, issues and solutions," in *Proc. Computer Vision and Pattern Recognition Workshop (CVPRW'04)*, Vol. 3, p. 35, IEEE Computer Society, New York (2004).
13. F. Xiao, J. M. DiCarlo, P. B. Catrysse, and B. A. Wandell, "Image analysis using modulated light sources," *Proc. SPIE* **430b**, 22–30 (2001).
14. R. Lange and P. Seitz, "Solid-state time-of-flight range camera," *IEEE J. Quantum Electron.* **37**(3), 390–397 (2001).
15. B. Buttgen, T. Oggier, R. Kaufmann, P. Seitz, and N. Blanc, "Demonstration of a novel drift field pixel structure for the demodulation of modulated light waves with application in three-dimensional image capture," *Proc. SPIE* **5302**, 9–20 (2004).
16. A. Ben-Israel and T. N. E. Greville, *Generalized Inverses*, Wiley, New York (1974).
17. Z. Xu, "Investigation of 3D-imaging systems based on modulated light and optical rf-interferometry (ORFI)," *ZESS Forschung*. **14**, 214 (1999); <http://www.shaker.de/Online-Gesamtkatalog/details.asp?ID=1328342&CC=35181&ISBN=3-8265-6736-6>.
18. T. Oggier, M. Lehmann, R. Kaufmann, M. Schweizer, M. Richter, P. Metzler, G. K. Lang, F. Lustenberger, and N. Blanc, "An all-solid-state optical range camera for 3D real-time imaging with sub-centimeter depth resolution (SwissRangerTM)," *Proc. SPIE* **5249**(65), 534–545 (2003).
19. W. C. Stone, M. Juberts, N. Dagalakakis, J. Stone, and J. Gorman, "Performance analysis of next-generation LADAR for manufacturing, construction, and mobility," *NIST Technical Report* (2004).
20. S. Beer, P. Zeller, N. Blanc, F. Lustenberger, and P. Seitz, "Smart pixels for real-time optical coherence tomography," *Proc. SPIE* **5302**, 21–32 (2004).
21. R. Ruocco, T. Shite White, and D. Jarrett, "Systematic errors in active 3D vision sensors," *IEE Proc. Vision Image Signal Process.* **150**(6), 341–345 (2003).
22. M. Lindner and A. Kolb, "Lateral and depth calibration of PMD-distance sensors," *Adv. Vis. Comput.* **2**, 524–533 (2006).
23. H. Rapp, M. Frank, F. A. Hamprecht, and B. Jähne, "A theoretical and experimental investigation of the systematic errors and statistical uncertainties of time-of-flight cameras," *Int. J. Intell. Syst. Technol. Appl.* **5**, 402–413 (1997).
24. P. Palojarvi, K. Maatta, and J. Kostamovaara, "Integrated time-of-flight laser radar," *IEEE Trans. Instrum. Meas.* **46**, 996–999 (1997).
25. J. W. Goodman, "Some effects of target-induced scintillation on optical radar performance," *Proc. IEEE* **53**(11), 1688–1700 (1965).
26. B. Schneider, "Der Photomischdetektor zur schnellen 3D-Vermessung für Sicherheitssysteme und zur Informationsübertragung im Automobil," Dr.-Ing Diss., Department of Electrical Engineering and Computer Science, University of Siegen (2003); [deposit.dbb.de/cgi-bin/dokserv?idn=970684355&dok\\_var=d1&dok\\_ext=pdf&filename=970684355.pdf](http://deposit.dbb.de/cgi-bin/dokserv?idn=970684355&dok_var=d1&dok_ext=pdf&filename=970684355.pdf).
27. J. Honerkamp, *Stochastic Dynamical Systems: Concepts, Numerical Methods, Data Analysis*, VCN, New York (1994).
28. K. V. Mardia and P. E. Jupp, *Directional Statistics*, Wiley Series in Probability and Statistics, Chichester (1999).
29. K. Iga, "Surface-emitting laser—its birth and generation of new optoelectronics field," *IEEE J. Sel. Top. Quantum Electron.* **6**(6), 1201–1215 (2000).
30. U. Seger, U. Apel, and B. Hoefflinger, "HDRC-imagers for natural visual perception," in *Handbook of Computer Vision and Application*, Vol. 1, pp. 223–235, Academic Press, Singapore (1999).



**Marlo Frank** studied physics at the Ruprecht-Karls-Universität Heidelberg and the University of Sydney. He passed with distinction in November 2007. During his studies, he worked as a student assistant with the Institute for Environmental Physics in Heidelberg. Being interested in environmental physics and medical physics at the beginning of his studies, his focus changed to image processing and machine learning while conducting his diploma thesis on the investigation of 3-D cameras. He is currently working on a PhD project at the Swiss Federal Institute of Technology (ETH) in Zurich. His research concerns unsupervised learning on discrete data structures with application to computer security.



**Matthias Plaue** studied physics in Heidelberg and Berlin with an emphasis on mathematical methods, in particular differential geometry and global analysis. Since 2007 he has been working toward his doctoral thesis at the Technische Universität (TU) Berlin in the field of Lorentzian geometry and mathematical cosmology while being active in a number of other projects including numerical analysis, 3-D face recognition, and mathematics education for engineers.



**Holger Rapp** studied physics at the University of Heidelberg. He conducted his diploma thesis concerning the TOF 3D camera systems, with the Image Processing Group of Bernd Jähne. He is currently a scholarship student in the Karlsruhe School of Optics and Photonics (KSOP) and working toward his PhD degree at the Karlsruhe Institute of Technology (KIT). His research interest there focuses on the practical application of optical physics in industry.



**Ullrich Köthe** received his diploma degree in physics from the University of Rostock in 1991 and his PhD degree in computer science from the University of Hamburg in 2000. He is a senior scientist with the Heidelberg Collaboratory for Image Processing. Prior to joining the University of Heidelberg, he was an assistant professor with the Cognitive Systems Group, University of Hamburg. His research interests include reliable image analysis methods, especially in the context of scientific imaging, the connection between image segmentation and machine learning, and generic software design for computer vision.



**Bernd Jähne** studied physics at the University of Saarbrücken and the University of Heidelberg. He received his diploma, doctoral, and habilitation degrees from Heidelberg University in 1977, 1980, and 1985, respectively, and a habilitation degree in applied computer science from the University of Hamburg-Harburg in 1992. In 1988 he became a marine research physicist with the Scripps Institution of Oceanography, University of California. Since 1994 he has

been a professor of physics with the Interdisciplinary Center of Scientific Computing (IWR) of Heidelberg University, heading research groups on image processing and small-scale air-sea interaction. Since 2008 he has also been coordinating director of the Heidelberg Collaboratory for Image Processing (HCI) and deputy director of the IWR. His research interests include small-scale air-sea interaction, imaging sensors, foundations of image and image sequence processing, and the application of image processing techniques in science and industry.



**Fred A. Hamprecht** studied chemistry with Swiss Federal Institute of Technology (ETH), and received his PhD degree from Zurich. After a brief period at the Seminar for Statistics, ETH Zurich, he became a Robert Bosch-endowed professor for Multidimensional Image Processing at the University of Heidelberg in 2001. He is a member of the Steering Committee of the German Association for Pattern Recognition (DAGM), and a cofounder of the Heidelberg

Collaboratory for Image processing (HCI). He is interested in all aspects of data analysis, ranging from signal and image processing to supervised, semisupervised, and unsupervised learning. With his group, he currently develops automated diagnostic systems with applications both in industrial quality control and the life sciences, where particular emphasis is put on user-friendly configuration and on a principled treatment of spatial and temporal context.